ACS APPLIED MATERIALS & INTERFACES

www.acsami.org Research Article

Wearable Exoskeleton System for Energy Harvesting and Angle Sensing Based on a Piezoelectric Cantilever Generator Array

Bingshan Hu,[¶] Jiangtao Xue,[¶] Dongjie Jiang, Puchuan Tan, Yiqian Wang, Minghao Liu, Hongliu Yu, Yang Zou,* and Zhou Li*

Cite This: https://doi.org/10.1021/acsami.2c08757 Read Online

ACCESS | Metrics & More | Article Recommendations | Supporting Information

ABSTRACT: Wearable exoskeletons are developing rapidly due to their superiority in improving human ability and efficiency. The construction of a multifunctional exoskeleton system relies on an efficient continuous energy supply and various high-performance sensors. Here, a magnetic-driven piezoelectric cantilever generator (MPCG) array is designed for energy harvesting and angle sensing of joint motions. Combining theoretical derivation and experimental characterization, it is found that the nonlinear magnetic force acting on the cantilever structure will cause the phenomenon of frequency upconversion, which greatly improves the output of the MPCG. The experiment successfully proves the feasibility of using the MPCG array as an energy-harvesting module to collect energy from human joint motions and power an RH/temp sensor. Furthermore, the MPCG array can also be used to sense the rotation angle and angular velocity. By integrating with a wireless data acquisition and transmission module and supporting software, a wearable joint rehabilitation monitoring and assessment system is built, which can measure the activities of the joint in real time and evaluate the flexion degree. The demonstrated wearable exoskeleton system for joint motion energy harvesting and joint angle sensing is of great value for the construction of a multifunctional exoskeleton system and wearable smart rehabilitation equipment.

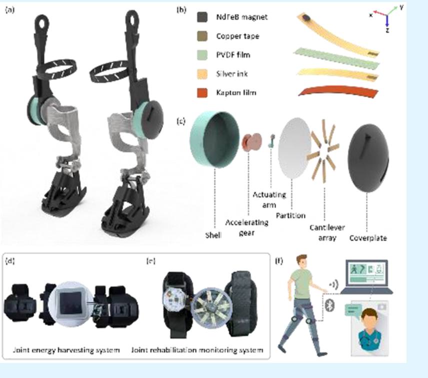

KEYWORDS: *wearable exoskeleton, cantilever structure, angular sensing, energy harvesting, frequency upconversion*

1. INTRODUCTION

The wearable exoskeleton is an electromechanical device that applies torque and force to the joints to assist the movement of human limbs, which is inspired by arthropods.[1−4] A wearable exoskeleton system is generally composed of a mechanical structure, sensor, actuator, and control system, integrating the technologies in the fields of mechanical engineering, electronics, automation, biomedicine, and so on.[5] The wearable exoskeleton was first applied in the military field to enhance soldiers' physical strength and endurance.[6,7] With the gradual growth of medical demand, the medical exoskeleton has become an important research field, which has attracted great interest due to its excellent efficacy in rehabilitation therapy.[8,9] The exoskeleton rehabilitation system can carry out rehabilitation training for people with movement disorders such as a stroke, spinal cord injury, and brain trauma.[10−12] In addition, with the development of intelligent robots, the exoskeleton also plays an important role in man−machine interaction.[5,13,14] Whether applied to health rehabilitation or man−machine interaction, various sensors such as angle sensors, pressure sensors, and myoelectric sensors need to be used in exoskeleton systems to obtain the posture, speed, force, and other physiological information on the wearer,[15] which means that additional energy input is required, increasing the power consumption, volume, mass, and cost of the equipment. Therefore, developing an energy conversion device that can harvest the energy of human motion or designing a self-powered sensor without needing an external power supply are promising strategies for the construction of wearable exoskeletal systems.

A triboelectric nanogenerator (TENG)[16−21] and piezoelectric nanogenerator (PENG)[22−26] can convert mechanical energy into electrical energy based on the triboelectric effect and piezoelectric effect, respectively. As emerging energy conversion technologies, TENGs and PENGs are flexible, highly efficient, simple to manufacture, low cost, and easy to integrate, which can provide a long-term power supply for sensing modules and other electronic components of the wearable exoskeleton system by collecting human motion energy, while they can also be used for fine sensing of human joint motion because of their outstanding mechanical response characteristics.[27−31] For example, Zhu et al.[32] developed a low-cost exoskeleton system based on TENGs that includes a

Received: May 17, 2022
Accepted: July 28, 2022

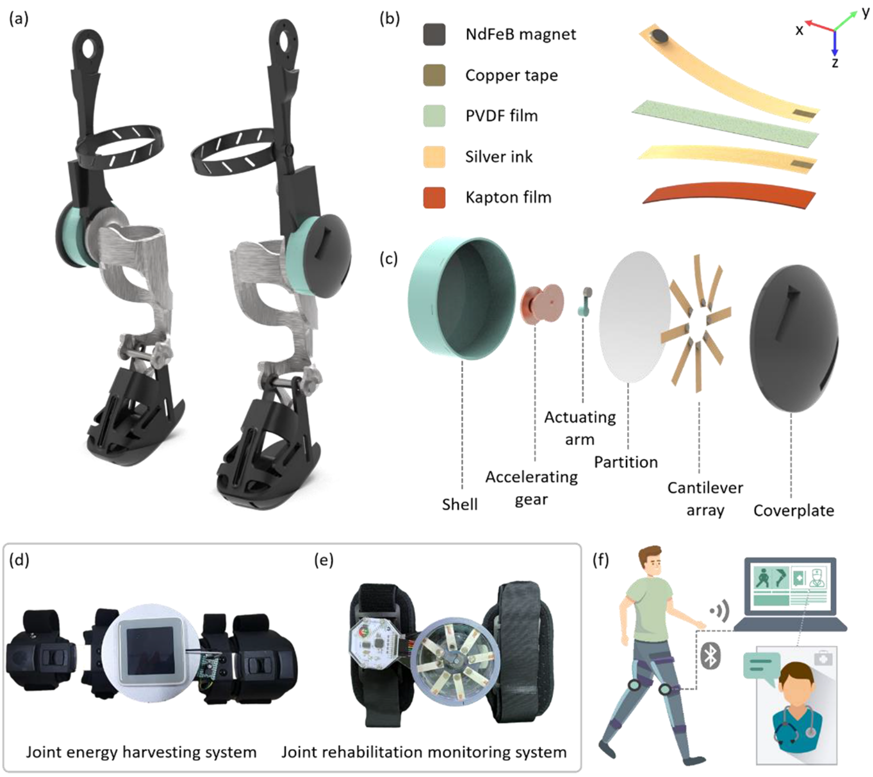

Figure 1. Structure and application of the wearable exoskeleton based on the MPCG. (a) Schematic diagram of a wearable exoskeleton system for the knee joint. (b) Exploded view of the MPCG. (c) Exploded view of the sensing module. (d) Photo of the joint energy-harvesting system. (e) Photo of the joint rehabilitation monitoring system. (f) Schematic diagram of wireless communication of a wearable exoskeleton system.

multidegree-of-freedom sensor capability for bidirectionally monitoring linear displacement, rotation, torsion, bending, and other movements. The sensing unit can realize the multidegree of freedom and multidimensional two-way motion sensing and solve the key technical problem of multidimensional motion sensing. Luo et al.[33] designed a modular, portable, and wearable knee brace system. The active joint range of motion is measured by using TENG with a rotating grid structure, and the isometric muscle force is measured by using a mechanical structure. The wearable system is designed with a minimum resolution of 0.01 N and 1°, respectively. Wang et al.[34] introduced two sets of generators with a coaxial arrangement and angle difference on the rotary table TENG, which can convert the rotating motion into a group of voltage signal outputs with a phase difference, and realized a self-powered angle sensor with nanoradian resolution for the wearable exoskeleton.

In this paper, a wearable exoskeleton system for energy harvesting and angle sensing of human joint motion is presented, which is based on a magnetic-driven piezoelectric cantilever generator (MPCG) array. The cantilever structure has a good response to external mechanical disturbance. Under the same excitation, the strain at the fixed end is large, and the polarization intensity of the piezoelectric layer is high.[35,36] As a result, the output of MPCG is high, which can be used for highly sensitive monitoring of joint movement. At the same time, the cantilever structure has the phenomenon of upfrequency conversion under the nonlinear magnetic drive, which greatly improves the output of the device.[37,38] After the eight-channel MPCG array is rectified in parallel, the 10 μF capacitor is charged to 3 V within 40 s, which can power RH/temp sensor. Furthermore, a joint rehabilitation monitoring system is developed by integrating the MPCG array and OpenBCI with a wearable exoskeleton. The joint motion signals can be collected by an MPCG array and recorded by OpenBCI and then transmitted to the supported analysis software by Bluetooth. The joint motion parameters such as angle and angular velocity can be displayed on the visual interface through waveform analysis, and the state of the joint can be evaluated by a pattern recognition algorithm.

2. RESULTS AND DISCUSSION

2.1. Overview of the Wearable Exoskeleton System Based on the MPCG. The wearable exoskeleton system based on a magnetic-driven piezoelectric cantilever generator (MPCG) is designed as shown in Figure 1a. The system consists of a sensing module, packing shells, and a wireless transmission device. The sensing module's main body is the MPCG array, which is made up of eight piezoelectric cantilever structures. The base layer of the cantilever is a 0.25 mm Kapton film; the piezoelectric layer is a 0.11 mm PVDF film coated with silver electrodes (Figure 1b); and the free end is attached with an N52 NdFeB magnet. The sensing module's excitation device is directly connected to the exoskeleton and is made up of two components: an accelerating gear and an actuating arm with an N52 magnet. The accelerating gear structure consists of a driving gear that is coaxially connected to the wearable exoskeleton and a driven gear that is connected to the actuating arm. They have the same modulus. The driven gear has six times as many teeth as the driving gear, so the transmission ratio is 1:6. The actuating arm rotates under the drive of the driven gear, which means that when the joint rotates 1° the actuating arm rotates 6°. At the joint, they are coaxial with the exoskeleton, meaning they rotate in lockstep

https://doi.org/10.1021/acsami.2c08757
ACS Appl. Mater. Interfaces XXXX, XXX, XXX−XXX

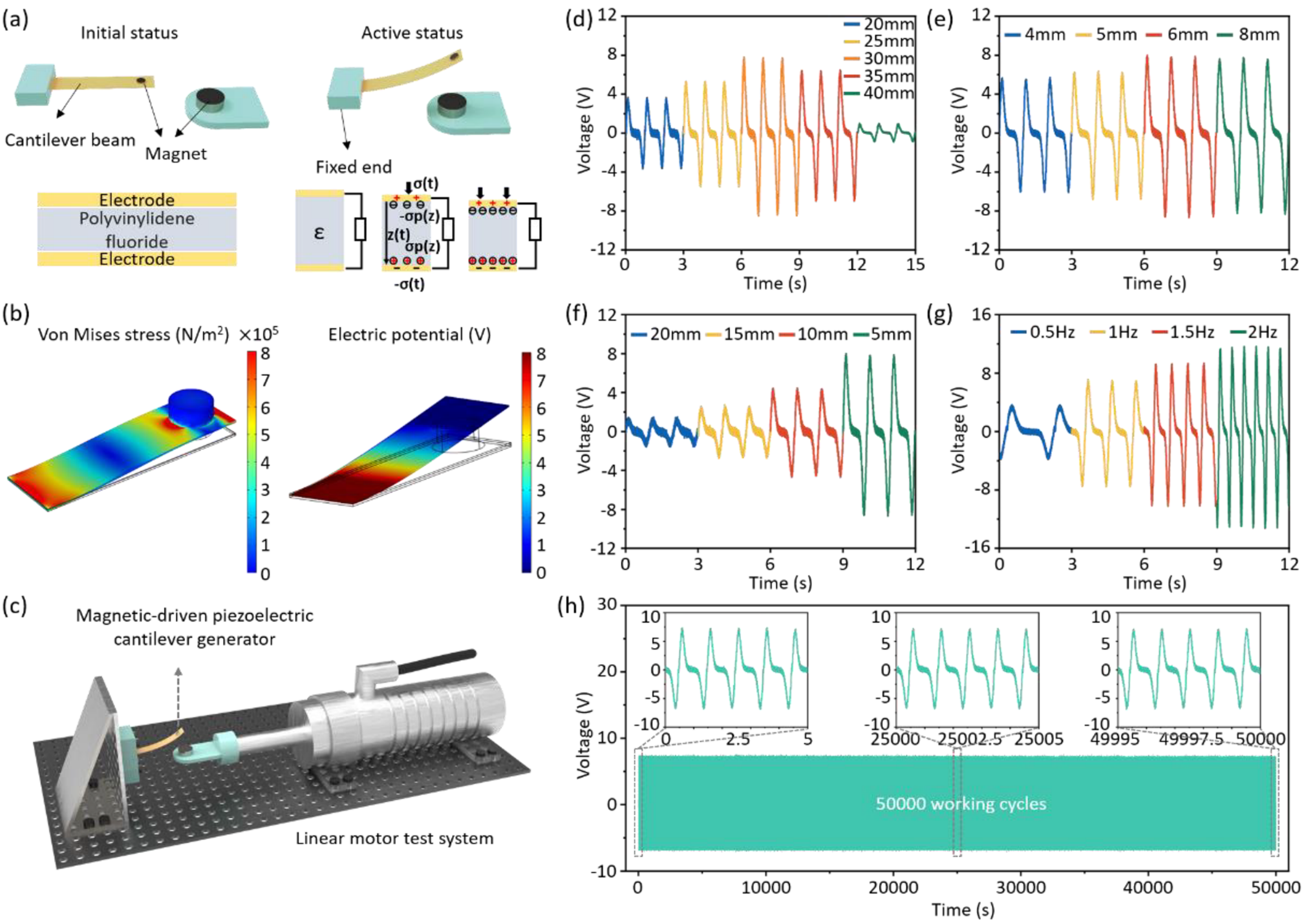

Figure 2. Characterization of the single MPCG. (a) Working principle of the single piezoelectric cantilever. (b) Mechanical and electrical simulation results of the piezoelectric cantilever beam by COMSOL Multiphysics. (c) Schematic diagram of the characterization test system. (d) Voltage signals under different piezoelectric cantilever beam lengths. (e) Voltage signals under different diameters of a free end magnet. (f) Voltage signals under different spacings between the free end magnetic and actuating arm. (g) Voltage signals under different excitation frequencies. (h) Fatigue characterization test data.

with the exoskeleton. The upper cover, middle baffle, and bottom shell comprise the package shells. The bottom shell holds the cantilever structure in place and connects the excitation module to the exoskeleton. The center baffle can keep the upper and lower magnets from colliding with each other during rotation due to attraction. The wireless transmission device collects the eight-channel sensor data and sends it through Bluetooth to the PC and other wireless devices.

The cantilever beam has a simple structure, a high-energy transmission ability, and a high sensitivity. It has the lowest resonance frequency and the most mechanical strain with the same structural size and load. As a result, it is frequently utilized in piezoelectric devices to harvest mechanical energy from the environment, such as vibration. The natural frequency of the cantilever structure is related to the geometric size of the structure, which will be proved in the following sections. However, they can only work at a very limited frequency, and the natural frequency of the cantilever structure under macrosize is usually relatively high, which cannot match the frequency of vibration in the external environment, resulting in a low output. At the free end of the cantilever structure, a mass block is usually added. On one hand, it can diminish the overall structure's stiffness and natural frequency. Simultaneously increasing the weight at the free end can improve the polarization of the piezoelectric layer in deformation, increasing the output and improving the sensitivity to external vibrations. In this paper, the magnet at the free end not only plays the role of the magnetic drive but also enhances the work done by inertial force. At the same time, this noncontact nonlinear magnetic drive brings magnetic plucking, causing the cantilever beam to create the phenomenon of upfrequency conversion, which is more favorable to the structure operating in a random low-frequency environment.

The sensing module uses noncontact magnetic force to trigger the deformation of the cantilever structure, avoiding the loss of power due to friction. The basic workflow is that the exoskeleton rotates to drive the coaxial excitation device to rotate. The polarity of the magnet on the actuating arm is the same as that of the free end of the cantilever to generate repulsive force. As a result, the piezoelectric cantilever structure deforms, resulting in a potential difference between the piezoelectric layer's upper and lower surfaces. The transmission device collects and analyzes data to determine the exoskeleton's rotation angle, direction, and speed and then sends it to the wireless device's APP interface (Figure 1f).

2.2. Theoretical Analysis and Characterization of the MPCG. The phenomenon of materials converting mechanical and electrical energy into each other is known as the piezoelectric effect, which occurs in asymmetric crystals.[25] The positive piezoelectric effect is used in piezoelectric sensors and energy harvesters. When mechanical stress is applied to a crystal, the structure deforms; the electric dipole moment shortens due to compression; and the piezoelectric material generates equal amounts of positive and negative charges on the surface to resist the change, resulting in polarization (Figure 2a). Magnetic excitation is used to drive the piezoelectric cantilever beam in this work. When two magnets are in close proximity, the cantilever deforms; the piezoelectric layer polarizes; and current is generated under external load. COMSOL Multiphysics is used to simulate a single cantilever structure, and the electromechanical coupling model is created and calculated by merging the solid mechanical and electrostatic fields (Figure 2b). When the cantilever structure is deformed, the stress is focused at the fixed end, as indicated in the diagram, and the polarization of the piezoelectric layer is primarily concentrated at that end.

In order to further explore the influencing factors of the resonant frequency of the cantilever structure, we characterize a single cantilever structure under different conditions. The vibration differential equation of the cantilever structure is established, and its frequency equation is solved by using the boundary condition of the cantilever beam. Assuming that every microsegment on the cantilever structure is moving periodically during the vibration process, the deflection of each point on the cantilever beam is

$$y(x, t) = Y = (x)\cos \omega t \tag{1}$$

where ω is the forced vibration frequency of the cantilever structure, and $Y(x)$ is the vibration modal function of the cantilever beam.

The microelement approach is used to determine the vibration differential equation of cantilever beam vibration, which is the balance between the elastic restoring force and inertial force

$$\frac{\partial^2}{\partial x}\left(EI\frac{\partial^2 y}{\partial x^2}\right)dx = -\frac{m_{\text{beam}}}{l}\frac{\partial^2 y}{\partial t^2}dx \tag{2}$$

where E is the Young's modulus; I represents the moment of inertia; and m_{beam} and l denote the mass and length of the cantilever beam, respectively. By introducing eq 1 into eq 2, the general solution of the vibration mode function $Y(x)$ can be obtained as

$$Y(x) = c_1 \sin\left(\frac{kx}{l}\right) + c_2 \cos\left(\frac{kx}{l}\right)c_3 \sinh\left(\frac{kx}{l}\right) + c_4 \cosh\left(\frac{kx}{l}\right) \tag{3}$$

where k is the frequency coefficient and the expression is

$$k = \sqrt[4]{\frac{\rho w h l^4 \omega^2}{EI}} \tag{4}$$

where w and h are the width and thickness of the cantilever structure, respectively.

In order to obtain the four coefficients in eq 3, the equation needs to be established according to the boundary conditions of the cantilever beam.

(1) Fixed end ($x = 0$): The displacement and rotation angle are zero.

$$Y = 0, \left.\frac{\partial Y}{\partial x}\right|_{x=0} = 0 \tag{5}$$

(2) Free end ($x = l$): The bending moment is equal to zero, and the shear force is equal to the inertial force generated when the tip magnet vibrates.

$$EI\left.\frac{\partial^2 Y}{\partial x^2}\right|_{x=1} = 0, \left.\frac{\partial}{\partial x}\left(EI\frac{\partial^2 y}{\partial x^2}\right)\right|_{x=1} = m_{\text{mag}}\left.\frac{\partial^2 y}{\partial t^2}\right|_{x=1} \tag{6}$$

where m_{mag} is the mass of the tip magnet.

The resonant frequency can be obtained by eq 4, which can be expressed as

$$\omega = \sqrt{\frac{EI}{\rho w h}}\frac{k^2}{l^2} \tag{7}$$

It can be seen from eq 8 that the resonant frequency is negatively correlated with the cantilever length and positively correlated with the frequency coefficient.

To get the frequency equation, substitute eqs 1 and 3 into eq 6

$$R_m k(-\sin k \cosh k + \cos k \sinh k) + \cos k \cosh k + 1 = 0 \tag{8}$$

where$R_m = \frac{m_{\text{mag}}}{m_{\text{beam}}}$. The value of k can be obtained by eq 8, and the relationship curve between the frequency coefficient k and mass ratio R_m can be seen in Figure S2, implying that the resonant frequency is negatively correlated with the magnet's mass. To summarize, the cantilever structure's resonance frequency is mostly determined by the length of the cantilever and the size of the free end magnet.

After obtaining the influencing factors of resonant frequency, the single MPCG is characterized. As shown in Figure 2c, the linear motor is used to drive the lower magnet to approach the upper magnet continuously, to deform the upper cantilever structure and generate electric potential. First, the output of the cantilever structure under different lengths is characterized. The excitation frequency of the linear motor is set as 1 Hz. Cantilever beams with different lengths are selected to test their output. Considering the size of the devices, five groups of lengths from 2 to 4 cm are selected for measurement and comparison. As shown in Figure 2d, it is found that with the increase of the length of the cantilever beam the open-circuit voltage first increases and then decreases. When the length is 30 mm, the strain of the cantilever structure is the largest. The rigidity of the structure diminishes as the beam length grows, and the output steadily rises; however, a too soft structure reduces resilience, lowering the device's output.

Then the influence of the size of the free end magnet on the output is explored (Figure 2e). The effect of the free end magnet's size on the output is then investigated. The thickness of the N52 magnet is 2 mm, and four sizes of magnets with diameters ranging from 4 to 8 mm were chosen. It was found that the size of the magnet has no obvious effect on the output. Finally, a magnet with a diameter of 6 mm was chosen.

After determining the size of the cantilever structure, the influence of different magnet spacing and different external excitation frequencies on the output is further explored (Figure

https://doi.org/10.1021/acsami.2c08757
ACS Appl. Mater. Interfaces XXXX, XXX, XXX−XXX

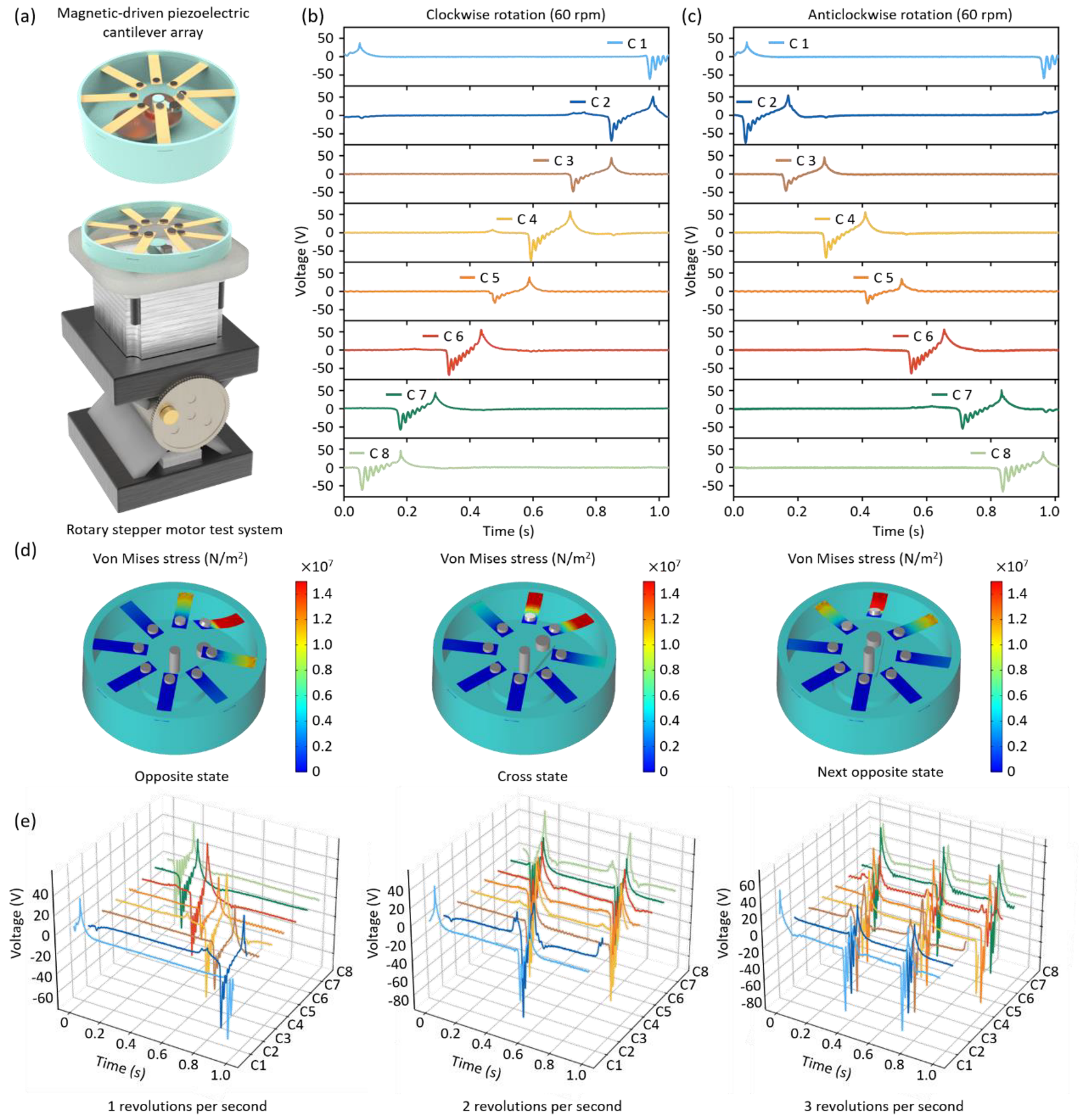

Figure 3. Characterization of the MPCG array. (a) Schematic diagram of the magnetic-driven piezoelectric array and characterization test system. (b) Eight-channel voltage waveforms under 60 rpm clockwise rotation. (c) Eight-channel voltage waveforms under 60 rpm anticlockwise rotation. (d) Stress simulation calculation results by COMSOL Multiphysics. (e) Eight-channel voltage waveforms under different rotating speeds.

2f, Figure 2g). The results show that the output of the device increases with the decrease of magnet spacing and the increase of frequency. Finally, the fatigue test of a single device is carried out (Figure 2h), and the results show that the output voltage of MPCG has not changed significantly after 50 000 cycles of operation.

2.3. Design and Characterization of an Eight-Channel MPCG Array. The structure of the eight-channel magnetic-driven piezoelectric cantilever generator (MPCG) array is shown in Figure 3a. The angle between each cantilever structure is 45°. For every 45° of rotation of the actuating arm, a cantilever structure will deform under the action of magnetic force and generate an electrical pulse. Thanks to the acceleration gear (transmission ratio 1:6), when the MPCG array is integrated with an exoskeleton, every 7.5° of joint rotation will cause the actuating arm to rotate 45°, and then a new electrical pulse will be generated. Finite element simulation for the MPCG array is carried out. It can be seen from Figure 3d that when the actuating arm is located below a cantilever the cantilevers on both sides will also be affected by the complex magnetic field (Figure S1) and deform to a certain extent. The deformation process of the eight-channel MPCG array during rotation can be seen in Video S1 of the Supporting Information. Under the action of complex

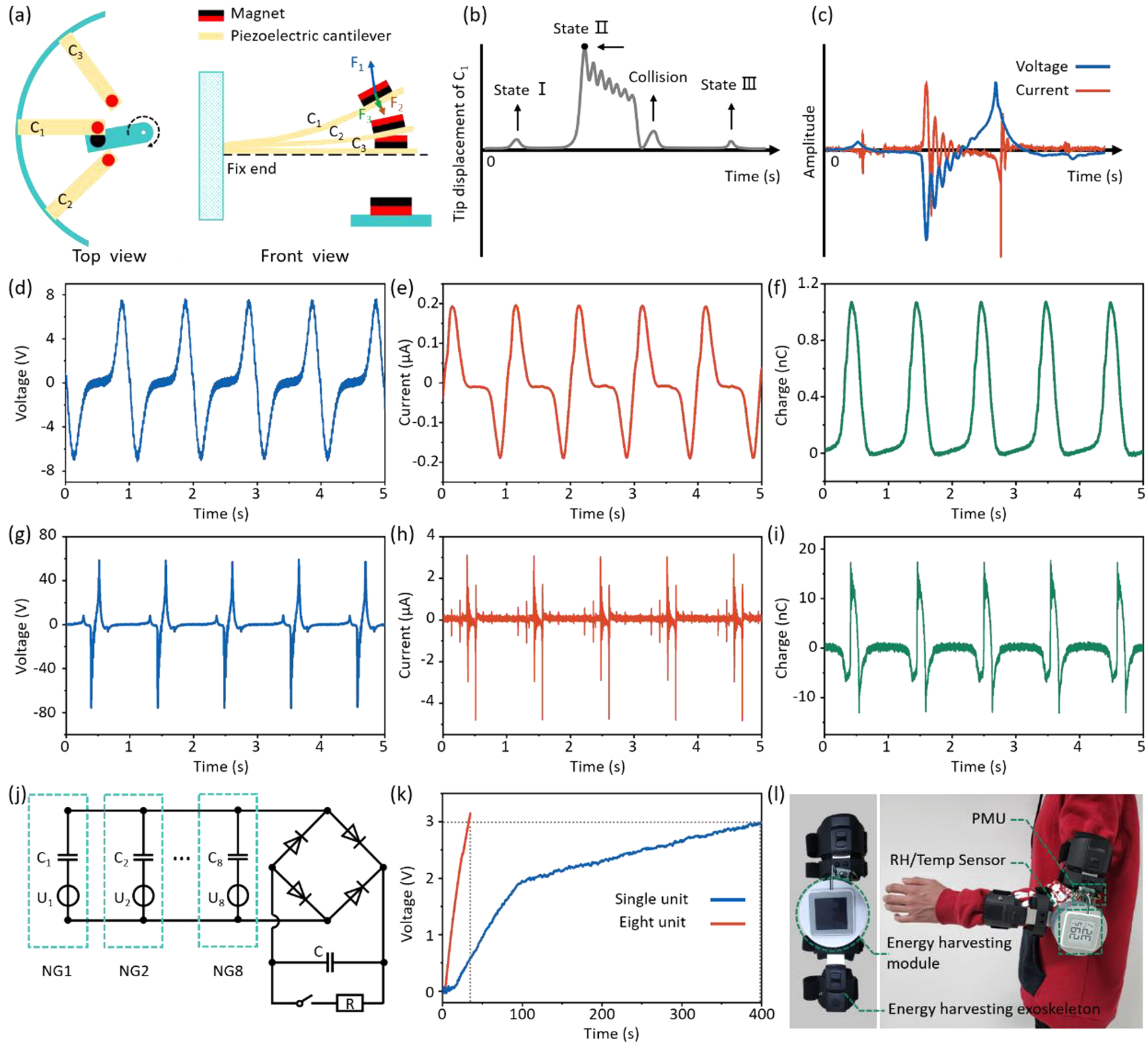

Figure 4. Power generation performance characterization of the energy-harvesting module. (a) Schematic diagram of the magnetic force on a free end magnet. (b) Schematic diagram of a free end displacement waveform. (c) Single-cycle voltage and current waveform with frequency upconversion phenomenon. (d−f) Waveform diagram of voltage, current, and charge without the frequency upconversion phenomenon. (g−i) Waveform diagram of voltage, current, and charge with frequency upconversion phenomenon. (j) Equivalent circuit diagram of the energy acquisition module. (k) Comparison diagram of eight units and single unit charging a 10 μF capacitor. (l) Application demonstration of integrating the charging module on the exoskeleton.

magnetic force, the magnet on the cantilever and the magnet on the actuating arm will easily collide or adsorb during the rotation of the actuating arm. Therefore, we have added an acrylic partition layer between the actuating arm and the cantilever, which can not only keep the initial state of the cantilever in the same horizontal plane under the action of complex magnetic force but also ensure the position between the magnets during the rotation.

The rotary stepper motor test system is used to characterize the magnetic-driven piezoelectric cantilever array. We set the initial position of the actuating arm as directly below the No. 1 piezoelectric cantilever beam. In the initial state, the No. 1 piezoelectric cantilever is in the active status. The rotation angle of the motor is set to 60°, and the rotation speed is 10 rpm. The rotation angle of the actuating arm is 360°, and the rotation speed is 60 rpm. The outputs of each channel under clockwise and counterclockwise rotation are measured, respectively, as shown in Figure 3b and Figure 3c. It can be seen from the figure that since the No. 1 piezoelectric cantilever is in the active status at the beginning there will be an upward peak at the beginning of the rotation process of Channel 1, while other channels have both upward and downward peaks in a cycle. It is due to the No. 1 cantilever being in the active status initially, and the upward peak is the electrical signal generated by the cantilever from the active status to the initial status and then colliding with the partition layer when the actuating directly below leaves. The downward peak is the electrical signal brought by the cantilever changing from the initial status to the active status when the actuating arm turns directly below the piezoelectric cantilever. Therefore, the rotation angular velocity of the actuating arm can be obtained by calculating the time difference between adjacent

https://doi.org/10.1021/acsami.2c08757
ACS Appl. Mater. Interfaces XXXX, XXX, XXX−XXX

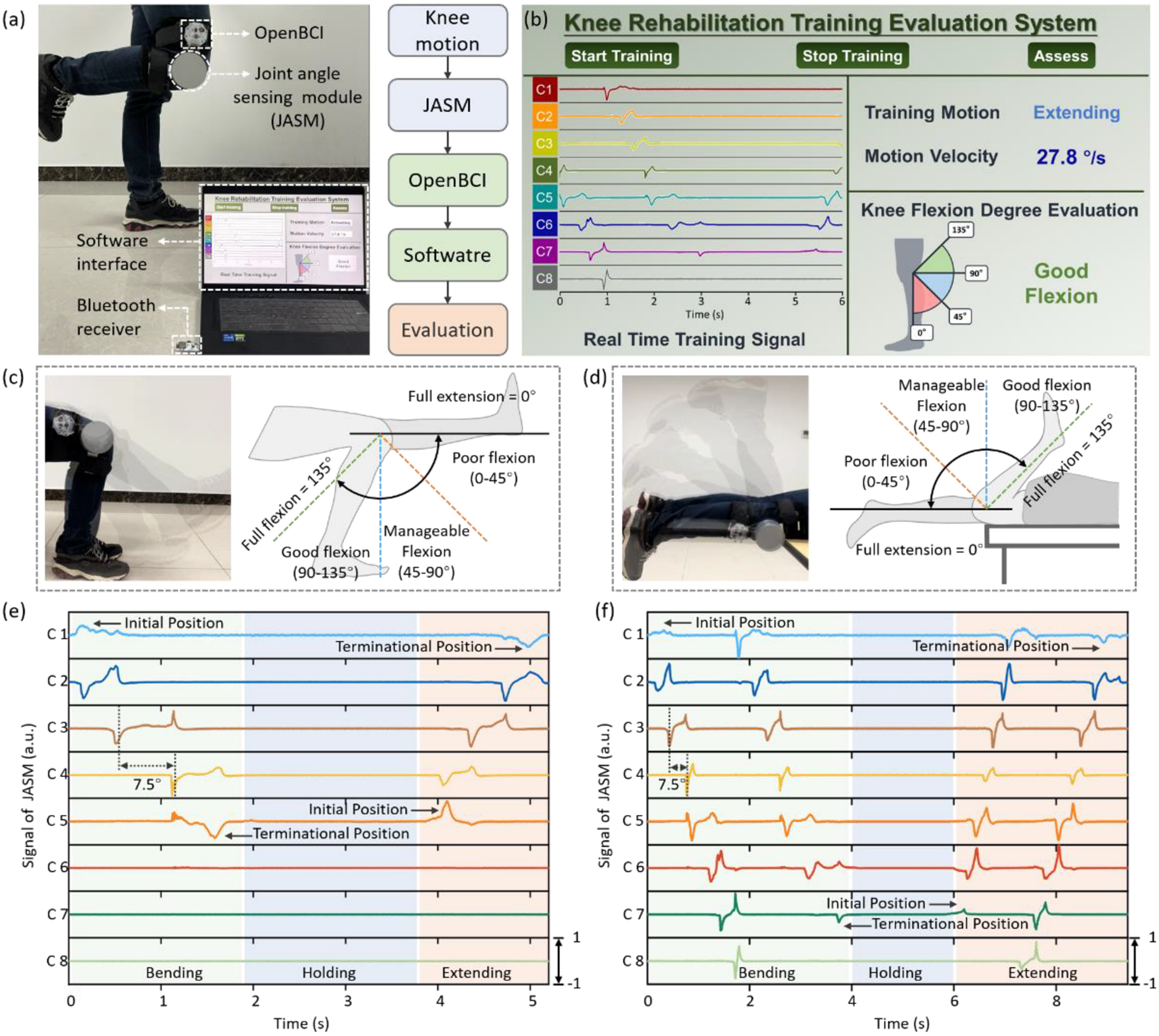

Figure 5. Joint rehabilitation training monitoring and analysis system. (a) Schematic diagram of the whole system. (b) The software interface of the system. (c), (e) Schematic diagram of knee joint bending and eight-channel waveform diagrams of subjects in the sitting state. (d), (f) Schematic diagram of knee joint bending and eight-channel waveform diagrams of subjects in the lying state.

downward peaks, and then the speed of the motor can be obtained.

At the same time, it can be seen that when the actuating arm passes directly under the cantilever the frequency of the vibration will rise, resulting in many small peaks. This is due to the frequency upconversion phenomenon caused by nonlinear magnetic force, which converts the original 1 Hz rotation into a high-frequency vibration of the cantilever structure. As shown in Figure 3b and Figure S4, the phenomenon only occurs in the first half of each cycle because the cantilever structure in the first half of the cycle is only driven by the nonlinear magnetic force, resulting in frequency upconversion vibration. After the collision between the cantilever beam and the partition layer, the energy of the vibration is absorbed rapidly, and the frequency upconversion phenomenon disappears. The contact between the cantilever structure and the partition layer results in a rapid change in the direction and speed of motion, resulting in a sudden increase in the strain at the fixed end of the cantilever structure, which in turn produces peak electrical signals after the collision. The stronger the frequency up effect (the higher the vibration frequency), the higher the output of the corresponding channel, as can be observed from the comparison. This is because the cantilever structure's resonant frequency is higher than the forced vibration's excitation frequency. The closer the cantilever's forced vibration frequency is to the structure's resonant frequency after frequency upconversion, the larger the deformation, the greater the strain at the fixed end, and the higher the polarization intensity. The output of the device under different frequencies is tested, respectively (Figure 3e). It can be seen that the waveform of each channel will not be affected by the change of frequency, which proves the stability of the device under different frequencies. The fatigue test of the eight-channel MPCG array was also carried out, and the

https://doi.org/10.1021/acsami.2c08757
ACS Appl. Mater. Interfaces XXXX, XXX, XXX−XXX

results show that the output voltage of the MPCG array has not changed significantly after 30 000 cycles of operation (Figure S3).

2.4. Wearable Exoskeleton Energy-Harvesting System. In order to further understand and verify the frequency conversion phenomenon, first, the stress and deformation of the MPCG are analyzed. As can be seen from Figure 4a, when the actuating arm rotates to different positions, the forces on different cantilever structures are also different. In the position shown in the figure, C_1 is not only repulsed by the actuating arm magnet but also attracted by C_2 and C_3. C_1 is the most repelled by the actuating arm in the position depicted in the diagram; hence, its deformation is the greatest. C_2 and C_3 will also be affected to some extent at the same time. Figure 4b shows a schematic diagram of the displacement of the magnet at the free end of the cantilever C_1 in a single cycle. The first small peak is the small displacement caused by the influence of the actuating arm on C_1 when it passes directly below C_2 (State I). When the actuating arm comes below C_1 (State II), the plucking of nonlinear magnetic force causes it to generate up-frequency conversion. When the actuating arm leaves C_1, it falls rapidly under the action of gravity and surrounding attractive magnetic force. When it reaches the partition layer, it collides and rebounds for a short period, so the second small peak will be generated. The third small peak is the displacement caused by the influence of the actuating arm when it is turned to C_3 (State III). From the waveform of voltage and current in Figure 4c, it can be seen that the instantaneous change of vibration velocity direction caused by collision produces great stress at the fixed end and produces a reverse peak. The output data of a single MPCG with a frequency upconversion effect can be seen in the Supporting Information (Figure S4). It is proven that the introduction of the partition layer can not only protect the equipment but also improve its output due to the collision of the piezoelectric cantilever beam. When characterizing a single cantilever structure in the previous section, the actuating arm was moved from far to near to excite the deformation of the cantilever, while the actuating arm used in the energy-harvesting module is close to the piezoelectric cantilever array from the beginning, and the periodicity of nonlinear magnetic force in the rotation process is similar to plucking the cantilever at the free end, resulting in frequency upconversion. The comparisons from Figure 4d to Figure 4i show that the output is significantly improved. The output voltage, current, and power density of MPCG with a series of loading resistance from 100 Ω to 10^9 Ω are shown in Figure S5. When the load is 10 MΩ, the power density of the MPCG can reach about 350 mW/m^2.

In order to verify the energy-harvesting module's power generation capacity, a power management circuit is designed as shown in Figure 4j. Eight MPCGs are connected in parallel and then connected in series with the rectifier bridge to charge a capacitor, and the circuit is controlled by the reed switch. The charging effect is compared with that of a single PENG (Figure 4k). It can be seen from the figure that the energy-harvesting module charges the 10 μF capacitor to 3 V within 40 s under the external excitation of 1 Hz, and the charging rate is about 10 times higher than that of a single PENG. Finally, we integrate the energy-harvesting module into the wearable exoskeleton device. A 100 μF capacitor was charged to 3 V within 7 min (Figure S6a) by collecting the energy of human activities. An RH/temp sensor is successfully powered by the energy-harvesting module (Figure 4l). The energy curve of the RH/temp sensor powered by the MPCG array is shown in Figure S6b, and it can be seen that a 100 μF capacitance is charged to 3 V within 300 s (under 1.5 Hz), which can power the RH/temp sensor to operate continuously for 100 s.

2.5. Joint Rehabilitation Monitoring and Assessment System. As mentioned above, the MPCG array has a good electrical response to the change in the rotation angle of the actuating arm. With the help of the accelerating gear, the device can be used for joint activity monitoring. Here, a joint rehabilitation monitoring and analysis system is presented, which is composed of a joint angle sensing module (JASM) based on the MPCG array, OpenBCI, and a data processing system written by Python software. Its workflow is shown in Figure 5a. When the joint moves, the sensing module moves to the data processing system through OpenBCI to calculate and analyze the parameters of the knee joint. The visual interface of the wireless PC terminal is shown in Figure 5b, and it shows the real-time waveform of eight channels, the state of joint activity, angular velocity, and the evaluation of joint rehabilitation based on the angle of joint activity. We divide the movable angle of the joint into three grades: 0−45° is poor flexion, 45−90° is manageable flexion, and greater than 90° is good flexion.

As shown in Figure 5c and 5d, by imitating the patient's knee rehabilitation training, we could select lying on front and sitting posture to perform joint bending and extending, respectively, and the activity state of the joint could be distinguished from the waveform of eight channels. The green area in the figure represents the bending movement of the joint. At this time, the peaks of the eight-channel waveform appear successively in the order of increasing the serial number of the channel. The red area represents the stretching movement of the joint, and the peaks of the corresponding eight-channel waveform appear in the order of decreasing the serial number. At the same time, it can be seen that the beginning and end of a joint activity status are marked by the half-cycle waveform of a certain channel. For example, in the process of joint bending in Figure 5e, the upward half-cycle waveform of Channel 1 marks the beginning of the bending movement, while the downward half-cycle waveform of Channel 5 marks the end of the bending movement. As mentioned in the previous section, the upward peak represents that the actuating arm stays directly below the cantilever, and the downward peak represents that it reaches directly below the cantilever. Therefore, the bending process in Figure 5e is the process of the actuating arm from under cantilever 1 to under cantilever 5. The angle between two adjacent cantilevers is 45°, and the transmission ratio of the accelerating gear is 1:6; therefore, the two peaks represent that the knee joint has turned 7.5°, which means that the angular resolution of the angle sensing module is 3.75° corresponding to half a cycle with the help of an accelerating gear with a magnification of 6 times. In the figure, three complete cycles plus two half-cycles constitute four complete cycles, so the joint has turned 30°. Similarly, it can be calculated that the knee joint in Figure 5f has turned about 105°. Then, the subjects were asked to simulate different levels of rehabilitation training (30° for poor flexion, 60° for manageable flexion, and 100° for good flexion) while standing and did three groups of knee joint bending and stretching reciprocating movements, respectively. The test process and the interface of evaluation software can be seen in Video S2 of Supporting Information. The data of a multicycle

https://doi.org/10.1021/acsami.2c08757
ACS Appl. Mater. Interfaces XXXX, XXX, XXX−XXX

random rehabilitation training action performed by the subjects in the standing state were also obtained (Figure S7).

3. CONCLUSIONS

In summary, a wearable exoskeleton system for energy harvesting and angle sensing of human joint motion is presented based on the MPCG. The cantilever structure is selected due to its high energy transmission capacity and sensitivity to vibration. After the theoretical derivation of the factors affecting the natural frequency of the piezoelectric cantilever structure, the different sizes of MPCG are characterized, and the optimal size is selected. In the experimental data of the sensing module based on the MPCG, the information on joint motion including rotation direction, angle, and angular velocity can be obtained through waveform analysis. At the same time, the phenomenon of frequency upconversion is found to be caused by the nonlinear magnetic force acting on the cantilever structure, which greatly improves the output of the piezoelectric cantilever beam. In order to determine the impact of this phenomenon on the performance of power generation, the charging performance of the MPCG array with a frequency upconversion effect is further explored. The energy-harvesting module constructed by integrating the MPCG array with a power management circuit can charge a 10 μF capacitor to 3 V in 40 s under 1 Hz excitation, and the wearable exoskeleton system based on the energy-harvesting module successfully collects the energy of joint activities for powering an RH/temp sensor. Furthermore, the MPCG array can also be used as a self-powered sensing module and a wearable joint rehabilitation monitoring and assessment system based on how the MPCG array is presented, which can wirelessly transmit the sensing data to the supported software, display joint motion information in real-time, and evaluate the flexion degree of the joint. The transmission ratio of the accelerating gear used in this work is 1:6, and when the transmission ratio is increased by designing a multilevel accelerating gear structure, it can further improve the energy collection efficiency of the energy-harvesting module, meanwhile improving the angular resolution of the angle-sensing module. The demonstrated wearable exoskeleton system for energy harvesting and angle sensing offers significant application potential for man−machine interaction and medical rehabilitation.

4. EXPERIMENTAL SECTION

4.1. Fabrication of the MPCG Array. Kapton film (35 mm × 10 mm × 0.25 mm) was selected as the base layer, and PVDF film (35 mm × 10 mm × 0.11 mm) coated with silver electrodes was adhered to the Kapton surface by VHB tape (composed of polyacrylate) after 0.08 mm diameter copper wires were attached to the silver electrodes on both sides of the PVDF. The N52 magnet (ϕ6 mm × h2 mm) was glued to one end of the strip PVDF with the single-component UV-curable adhesive, while the other end was glued to the hole reserved on the 3D-printed shell with the single-component UV-curable adhesive. The glue was cured with UV light for 30 s. The above process was the process of preparing a single MPCG. Then eight MPCGs were glued in turn and fixed to the shell to form the MPCG array.

4.2. Characterization and Measurements. An oscilloscope (LeCroy, HDO6104) was used for measuring the open-circuit voltage of the MPCG array and storing the data. An electrometer (Keithley 6517) was used for measuring the current and charge of MPCG and the energy-harvesting module. A linear motor (LinMot E1100) was used to characterize a single MPCG. The distance between magnets and the frequency of excitation was changed by controlling the displacement, speed, and acceleration of the linear motor. A rotating stepper motor was used to characterize the MPCG array, and the speed and rotation angle can be directly adjusted manually.

■ ASSOCIATED CONTENT

Supporting Information

The Supporting Information is available free of charge at https://pubs.acs.org/doi/10.1021/acsami.2c08757.

Magnetic field distribution when the actuating arm is directly below C_1 (Figure S1); the relationship curve between the frequency coefficient k and mass ratio R_m (Figure S2); fatigue characterization test data of an eight-channel MPCG array (Figure S3); the output data of a single MPCG with a frequency upconversion effect (Figure S4); output of MPCG with various loading resistances (Figure S5); charging performance of the energy-harvesting module (Figure S6); and multicycle-simulated rehabilitation training in the standing state (Figure S7) (PDF)

Stress distribution simulation by COMSOL Multiphysics (AVI)

Real-time joint rehabilitation monitoring and analysis system based on the MPCG array (MP4)

■ AUTHOR INFORMATION

Corresponding Authors

Yang Zou − *CAS Center for Excellence in Nanoscience, Beijing Key Laboratory of Micro-nano Energy and Sensor, Beijing Institute of Nanoenergy and Nanosystems, Chinese Academy of Sciences, Beijing 101400, China; Institute of Engineering Medicine, School of Life Science, Beijing Institute of Technology, Beijing 100081, China*; Email: zouyang@binn.cas.cn

Zhou Li − *CAS Center for Excellence in Nanoscience, Beijing Key Laboratory of Micro-nano Energy and Sensor, Beijing Institute of Nanoenergy and Nanosystems, Chinese Academy of Sciences, Beijing 101400, China; School of Nanoscience and Technology, University of Chinese Academy of Sciences, Beijing 100049, China; Center on Nanoenergy Research, School of Mechanical Engineering, School of Physical Science and Technology, Guangxi University, Nanning 530004, China*; orcid.org/0000-0002-9952-7296; Email: zli@binn.cas.cn

Authors

Bingshan Hu − *Institute of Rehabilitation Engineering and Technology, University of Shanghai for Science and Technology, Shanghai 200093, China*

Jiangtao Xue − *CAS Center for Excellence in Nanoscience, Beijing Key Laboratory of Micro-nano Energy and Sensor, Beijing Institute of Nanoenergy and Nanosystems, Chinese Academy of Sciences, Beijing 101400, China; Institute of Engineering Medicine, School of Life Science, Beijing Institute of Technology, Beijing 100081, China*

Dongjie Jiang − *CAS Center for Excellence in Nanoscience, Beijing Key Laboratory of Micro-nano Energy and Sensor, Beijing Institute of Nanoenergy and Nanosystems, Chinese Academy of Sciences, Beijing 101400, China; School of Nanoscience and Technology, University of Chinese Academy of Sciences, Beijing 100049, China*

Puchuan Tan − *CAS Center for Excellence in Nanoscience, Beijing Key Laboratory of Micro-nano Energy and Sensor,*

https://doi.org/10.1021/acsami.2c08757
ACS Appl. Mater. Interfaces XXXX, XXX, XXX−XXX

Beijing Institute of Nanoenergy and Nanosystems, Chinese Academy of Sciences, Beijing 101400, China; School of Biological Science and Medical Engineering, Beihang University, Beijing 100191, China

Yiqian Wang − *CAS Center for Excellence in Nanoscience, Beijing Key Laboratory of Micro-nano Energy and Sensor, Beijing Institute of Nanoenergy and Nanosystems, Chinese Academy of Sciences, Beijing 101400, China; Center on Nanoenergy Research, School of Mechanical Engineering, School of Physical Science and Technology, Guangxi University, Nanning 530004, China*

Minghao Liu − *CAS Center for Excellence in Nanoscience, Beijing Key Laboratory of Micro-nano Energy and Sensor, Beijing Institute of Nanoenergy and Nanosystems, Chinese Academy of Sciences, Beijing 101400, China; Center on Nanoenergy Research, School of Mechanical Engineering, School of Physical Science and Technology, Guangxi University, Nanning 530004, China*

Hongliu Yu − *Institute of Rehabilitation Engineering and Technology, University of Shanghai for Science and Technology, Shanghai 200093, China*

Complete contact information is available at:
https://pubs.acs.org/10.1021/acsami.2c08757

Author Contributions

[¶]B.H. and J.X. contributed equally to this work.

Author Contributions

B.H. and J.X. contributed equally. Z.L. and Y.Z. supervised the project. B.H., J.X., and Y.Z. conceived the idea and designed the experiments. B.H., J.X., Y.Z., and D.J. fabricated the devices. J.X., D.J., P.T., Y.W., and M.L. conducted the device performance characterization. J.X., Y.Z., and H.Y. wrote the article, and all authors reviewed and commented on the article. All authors have given approval to the final version of the article.

Notes

The authors declare no competing financial interest.

■ ACKNOWLEDGMENTS

Z.L. received funding from the National Natural Science Foundation of China (61875015, T2125003), Beijing Natural Science Foundation (JQ20038), and the Strategic Priority Research Program of Chinese Academy of Sciences (XDA16021101). Y.Z. received funding from the National Postdoctoral Program for Innovative Talent (BX20220380) and China Postdoctoral Science Foundation (2022M710389). B.H. received funding from the Natural Science Foundation of Shanghai China (20ZR1437800). The authors thank everyone who contributed to this work.

■ REFERENCES

(1) Pons, J. L. *Wearable Robots: Biomechatronic Exoskeletons*; John Wiley & Sons, 2008.

(2) Bai, S.; Virk, G. S.; Sugar, T. G. *Wearable Exoskeleton Systems: Design, Control and Applications*; Institution of Engineering and Technology, 2018.

(3) Gull, M. A.; Bai, S.; Bak, T. A Review on Design of Upper Limb Exoskeletons. *Robotics* **2020**, *9* (1), 16.

(4) Chen, B.; Ma, H.; Qin, L.-Y.; Gao, F.; Chan, K.-M.; Law, S.-W.; Qin, L.; Liao, W.-H. Recent Developments and Challenges of Lower Extremity Exoskeletons. *J. Orthop. Transl.* **2016**, *5*, 26−37.

(5) Anam, K.; Al-Jumaily, A. A. Active Exoskeleton Control Systems: State of the Art. *Procedia Eng.* **2012**, *41*, 988−994.

(6) Kumar, V.; Hote, Y. V.; Jain, S. Review of Exoskeleton: History, Design and Control. In *2019 3rd International Conference on Recent Developments in Control, Automation & Power Engineering (RDCAPE)*; IEEE, 2019; pp 677−682.

(7) Yu, S.; Han, C.; Cho, I. Design Considerations of a Lower Limb Exoskeleton System to Assist Walking and Load-Carrying of Infantry Soldiers. *Appl. Bionics Biomech.* **2014**, *11* (3), 119−134.

(8) de la Iglesia, D. H.; Mendes, A. S.; González, G. V.; Jiménez-Bravo, D. M.; de Paz Santana, J. F. Connected Elbow Exoskeleton System for Rehabilitation Training Based on Virtual Reality and Context-Aware. *Sensors* **2020**, *20* (3), 858.

(9) Stopforth, R. Customizable Rehabilitation Lower Limb Exoskeleton System. *Int. J. Adv. Robot. Syst.* **2012**, *9* (4), 152.

(10) Ou, Y.-K.; Wang, Y.-L.; Chang, H.-C.; Chen, C.-C. Design and Development of a Wearable Exoskeleton System For Stroke Rehabilitation. *Healthcare* **2020**, *8*, 18.

(11) Bogue, R. Robotic Exoskeletons: A Review of Recent Progress. *Ind. Robot* **2015**, *42* (1), 5−10.

(12) He, Y.; Eguren, D.; Luu, T. P.; Contreras-Vidal, J. L. Risk Management and Regulations for Lower Limb Medical Exoskeletons: a Review. *Med. Devices: Evidence Res.* **2017**, *10*, 89.

(13) Huang, R.; Cheng, H.; Guo, H.; Lin, X.; Zhang, J. Hierarchical Learning Control with Physical Human-Exoskeleton Interaction. *Inf. Sci.* **2018**, *432*, 584−595.

(14) Duong, M. K.; Cheng, H.; Tran, H. T.; Jing, Q. Minimizing Human-Exoskeleton Interaction Force Using Compensation for Dynamic Uncertainty Error with Adaptive RBF Network. *J. Intell. Robotic Syst.* **2016**, *82* (3), 413−433.

(15) Young, A. J.; Ferris, D. P. State of the Art and Future Directions for Lower Limb Robotic Exoskeletons. *IEEE T. Neur. Sys. Reh.* **2017**, *25* (2), 171−182.

(16) Fan, F.-R.; Tian, Z.-Q.; Lin Wang, Z. Flexible Triboelectric Generator. *Nano energy* **2012**, *1* (2), 328−334.

(17) Wang, S.; Lin, L.; Wang, Z. L. Nanoscale Triboelectric-Effect-Enabled Energy Conversion for Sustainably Powering Portable Electronics. *Nano Lett.* **2012**, *12* (12), 6339−6346.

(18) Fan, F.-R.; Lin, L.; Zhu, G.; Wu, W.; Zhang, R.; Wang, Z. L. Transparent Triboelectric Nanogenerators and Self-powered Pressure Sensors Based on Micropatterned Plastic Films. *Nano Lett.* **2012**, *12* (6), 3109−3114.

(19) Zhang, C.; Zhou, L.; Cheng, P.; Yin, X.; Liu, D.; Li, X.; Guo, H.; Wang, Z. L.; Wang, J. Surface Charge Density of Triboelectric Nanogenerators: Theoretical Boundary and Optimization Methodology. *Appl. Mater. Today* **2020**, *18*, 100496.

(20) Ryu, H.; Park, H.-m.; Kim, M.-K.; Kim, B.; Myoung, H. S.; Kim, T. Y.; Yoon, H.-J.; Kwak, S. S.; Kim, J.; Hwang, T. H. Self-Rechargeable Cardiac Pacemaker System with Triboelectric Nanogenerators. *Nat. Commun.* **2021**, *12* (1), 1−9.

(21) Liu, Y.; Liu, W.; Wang, Z.; He, W.; Tang, Q.; Xi, Y.; Wang, X.; Guo, H.; Hu, C. Quantifying Contact Status and the Air-Breakdown Model of Charge-Excitation Triboelectric Nanogenerators to Maximize Charge Density. *Nat. Commun.* **2020**, *11* (1), 1−8.

(22) Erturk, A.; Inman, D. J. *Piezoelectric Energy Harvesting*; John Wiley & Sons, 2011; p 314.

(23) Steinem, C.; Janshoff, A. *Piezoelectric Sensors*; Springer Science & Business Media, 2007; pp 8−10.

(24) Caliò, R.; Rongala, U. B.; Camboni, D.; Milazzo, M.; Stefanini, C.; De Petris, G.; Oddo, C. M. Piezoelectric Energy Harvesting Solutions. *Sensors* **2014**, *14* (3), 4755−4790.

(25) Zhang, H.; Zhang, X.-S.; Cheng, X.; Liu, Y.; Han, M.; Xue, X.; Wang, S.; Yang, F.; Smitha, A.; Zhang, H. A Flexible and Implantable Piezoelectric Generator Harvesting Energy from the Pulsation of Ascending Aorta: in Vitro and in Vivo Studies. *Nano Energy* **2015**, *12*, 296−304.

(26) Wang, X. Piezoelectric Nanogenerators—Harvesting Ambient Mechanical Energy at the Nanometer Scale. *Nano Energy* **2012**, *1* (1), 13−24.

(27) Zou, Y.; Liao, J.; Ouyang, H.; Jiang, D.; Zhao, C.; Li, Z.; Qu, X.; Liu, Z.; Fan, Y.; Shi, B. A Flexible Self-Arched Biosensor Based on

Combination of Piezoelectric and Triboelectric Effects. *Appl. Mater. Today* **2020**, *20*, 100699.

(28) Cao, Y.; Yang, Y.; Qu, X.; Shi, B.; Xu, L.; Xue, J.; Wang, C.; Bai, Y.; Gai, Y.; Luo, D. A Self-Powered Triboelectric Hybrid Coder for Human−Machine Interaction. *Small Methods* **2022**, *6*, 2101529.

(29) Jiang, D.; Ouyang, H.; Shi, B.; Zou, Y.; Tan, P.; Qu, X.; Chao, S.; Xi, Y.; Zhao, C.; Fan, Y. A Wearable Noncontact Free-Rotating Hybrid Nanogenerator for Self-Powered Electronics. *InfoMat* **2020**, *2* (6), 1191−1200.

(30) Liu, L.; Shi, Q.; Lee, C. A Hybridized Electromagnetic-Triboelectric Nanogenerator Designed for Scavenging Biomechanical Energy in Human Balance Control. *Nano Res.* **2021**, *14* (11), 4227−4235.

(31) Gao, S.; He, T.; Zhang, Z.; Ao, H.; Jiang, H.; Lee, C. A Motion Capturing and Energy Harvesting Hybridized Lower-Limb System for Rehabilitation and Sports Applications. *Adv. Sci.* **2021**, *8* (20), 2101834.

(32) Zhu, M.; Sun, Z.; Chen, T.; Lee, C. Low Cost Exoskeleton Manipulator Using Bidirectional Triboelectric Sensors Enhanced Multiple Degree of Freedom Sensory System. *Nat. Commun.* **2021**, *12* (1), 1−16.

(33) Luo, J.; Li, Y.; He, M.; Wang, Z.; Li, C.; Liu, D.; An, J.; Xie, W.; He, Y.; Xiao, W.; et al. Rehabilitation of Total Knee Arthroplasty by Integrating Conjoint Isometric Myodynamia and Real-Time Rotation Sensing System. *Adv. Sci.* **2022**, *9*, 2105219.

(34) Wang, Z.; An, J.; Nie, J.; Luo, J.; Shao, J.; Jiang, T.; Chen, B.; Tang, W.; Wang, Z. L. A Self-Powered Angle Sensor at Nanoradian-Resolution for Robotic Arms and Personalized Medicare. *Adv. Mater.* **2020**, *32* (32), 2001466.

(35) Lang, H. P.; Hegner, M.; Gerber, C. Cantilever Array Sensors. *Mater. Today* **2005**, *8* (4), 30−36.

(36) Boisen, A.; Thundat, T. Design & Fabrication of Cantilever Array Biosensors. *Mater. Today* **2009**, *12* (9), 32−38.

(37) Kuang, Y.; Yang, Z.; Zhu, M. Design and Characterisation of a Piezoelectric Knee-Joint Energy Harvester with Frequency Up-Conversion through Magnetic Plucking. *Smart Mater. Struct.* **2016**, *25* (8), 085029.

(38) Pillatsch, P.; Yeatman, E. M.; Holmes, A. S. A Piezoelectric Frequency Up-Converting Energy Harvester with Rotating Proof Mass for Human Body Applications. *Sens. Actuators, A* **2014**, *206*, 178−185.

https://doi.org/10.1021/acsami.2c08757
ACS Appl. Mater. Interfaces XXXX, XXX, XXX−XXX